VOL. 27, NO. 6 J. AIRCRAFT JUNE 1990

Strake Camber and Thickness Design Procedure for Low Alpha Supersonic Flow

James L. Pittman* and Daryl L. Bonhaus†
NASA Langley Research Center, Hampton, Virginia
and
Michael J. Siclari‡
Grumman Aerospace Corporation, Bethpage, New York

A procedure for the design of a strake mounted on a large forebody at a typical supersonic cruise condition is described. The design goal is attached flow on the upper surface of the strake at the low lift condition. Strake camber and thickness are systematically varied until an attached-flow, surface-pressure distribution is achieved. The surface pressures are computed by a full-potential solver, NCOREL, and an empirical guideline is used to prevent leading-edge flow separation. Experimental surface-pressures and flow-visualization data verified that the design goal was achieved. The high alpha flowfield is also investigated experimentally and computationally. A large vortex is observed above the strake leeside, and a pair of vortices is found on the forebody upper surface aft of the canopy. A shock that forms aft of the canopy probably causes the forebody vortices. The strake leading-edge vortex is predicted by an Euler method but not by the full-potential method. Experimental forces and pitching moment are well predicted by both computational methods, but the Euler pitching-moment predictions are clearly superior.

Introduction

Wing strakes appear on several current-generation, high-performance tactical aircraft (e.g., F-16, F-18, and Mig-29) to improve high lift capability at subsonic and transonic speeds. The efficiency of the strake is because of a strong, well-organized vortex that is created at the strake leading edge at high α. For improving $C_{L_{\max}}$, the additional planform area of the strake is more effective than adding the same area to the wing planform. A comprehensive discussion of strake aerodynamics at subsonic and transonic speeds is provided in Ref. 1.

Although current generation straked aircraft possess a supersonic dash capability, future aircraft mission scenarios emphasize efficient supersonic cruise to improve survivability.[2] It is also reasonable to assume that a maneuver capability will be required at supersonic conditions. For these reasons, it is important to develop an understanding of strake flowfields at supersonic speeds.

This study of strake aerodynamics in supersonic flow is conducted in two parts. The first part is a systematic computational design of the strake camber and thickness mounted on a large forebody, and the second part is the experimental validation of a design chosen from part 1. The computational design study is aimed exclusively at a typical supersonic cruise point, whereas the experimental study validates the computational results and explores the flowfield at a high angle of attack.

The computational design study focuses on a design point of Mach 1.80 and $\alpha = 4$ deg. The goal is to computationally design a cambered strake the would maintain attached flow on the strake upper surface at the design point. This design procedure requires a computational tool that accurately predicts pressures on the surface of the geometry, especially the critical leading-edge region, and an empirical criterion for preventing leading-edge separation. The computational tool selected is a three-dimensional, full-potential, supersonic marching code referred to as NCOREL.[3]

The configuration for this study is an idealized fighter-type forebody and strake with the aft body and wing truncated at the spanwise plane where the wing and strake would intersect. This approach simplifies the computational design effort and allows the construction of a large wind-tunnel model for experimental study. A large model is more suitable for extensive pressure instrumentation and permits accurate machining in the critical leading-edge region of the strake.

This paper describes the computational design study and the experimental validation. Results from the computational design study include geometry development and a description of the attached-flow pressure distribution that is used as the figure of merit for this study. Following a brief discussion of the wind-tunnel model design, experimental verification results are presented for low angle of attack by comparing experimental and full-potential surface-pressure data and by examining flow-visualization data. The high angle-of-attack flowfield is investigated similarly with additional predictions from an Euler solver. Finally, the full-potential and Euler surface-pressure predictions are integrated to compare lift, drag, and pitching-moment coefficients with experimental values.

Computational Design Study

Carefully choosing the proper tools for the stated problem directly relates to the success of any design effort. Choosing the proper computational tool requires knowledge of the following areas: 1) the physics of the flowfield, 2) the assumptions found in different mathematical models that describe fluid flow, and 3) the computer codes that solve these mathematical models. The rationale for selecting the NCOREL full-potential solver as the primary tool for this study is given below.

The design goal of maintaining attached flow on the upper surface of the highly swept strake requires a prediction

---

Presented as Paper 87-2638 at the AIAA 5th Applied Aerodynamics Conference, Monterey, CA, Aug. 17–19, 1987; received July 7, 1989; revision received Dec. 4, 1989.

*Aero-Space Technologist, Supersonic/Hypersonic Aerodynamics Branch, Applied Aerodynamics Division. Associate Fellow AIAA.

†Cooperative Education Student. Student Member AIAA.

‡Senior Research Scientist. Associate Fellow AIAA.

method that accurately computes surface pressures, especially in the critical leading-edge region. This requirement rules out linearized potential theory in favor of a nonlinear flow solver, which models either the full-potential, the Euler, or the Reynolds-averaged Navier-Stokes equations. Because the occurrence of separation is a viscous-dominated phenomenon, the Reynolds-averaged Navier-Stokes equations are the most appropriate flow model. However, solvers for this flow model are considered to be impractical tools for a parametric investigation involving a complex three-dimensional geometry.

Euler solvers have demonstrated an ability to model leading-edge separation for the special case of a highly swept, sharp leading-edge lifting surface[4,5] because of the numerical artificial viscosity that is required for stable numerical solutions. This study, however, considers rounded leading edges; therefore, Euler solvers cannot reliably predict leading-edge separation.

The design Mach number of 1.80 and the low α do not produce strong bow shocks, therefore an assumption of isentropic flow is valid. Consequently, a full-potential solver should provide a similar level of accuracy as an Euler solver with significantly reduced computational time. Because the full-potential equation does not model rotational flow, an empirical guideline must be used with the computed surface pressures to achieve the goal of specifying a strake camber and thickness that have attached upper-surface flow at the design point.

An attached-flow, surface-pressure distribution is not specified by a certain pressure level at each point on the surface but instead is characterized by the absence of strong flow gradients. The pressure distribution is examined in the spanwise plane because the flow gradients are strongest in this plane. At high α, suction pressure peaks at the leading edge and strong crossflow shocks on the upper surface must be avoided. For these study conditions, the crossflow remained subcritical and, consequently, crossflow shocks did not develop. The only empirical guideline this study required was simply to avoid large leading-edge suction peaks. Camber and leading-edge radius satisfy this guideline, which has been experimentally verified[6,7] for wing-alone geometries with sweep angles of 57 and 65 deg at Mach 1.62.

The physical issue of leading-edge flow separation is tied to the numerical issue of grid density. An insufficient number of grid points results in poor flowfield resolution. Therefore, the effects of grid density on the surface-pressure prediction must be examined. A crossflow grid density of 57 points around the half body and 57 points from the body surface (inner boundary) to the bow shock (outer boundary) provided an accurate resolution of surface pressures. The circumferential points were clustered by a cosine function near the strake leading edge because this was the region of strong flow gradients. The radial points were evenly spaced between the inner and outer boundaries, and the marching step size was approximately 3% of body length, yielding 1.17×10^5 grid points.

The geometry investigated in this effort can be described as an idealized, advanced fighter forebody and a body-mounted wing strake. The forebody, the strake planform, and the intersection lines of the strake with the body were held constant. The strake thickness distribution and camber surface were varied systematically to achieve an attached-flow pressure distribution. An inverse full-potential method does not exist for supersonic flow; therefore, the design study became a design-by-iteration process. An analytic geometry specification is highly beneficial because this allows the rapid creation of many geometries for analysis.

A family of strake camber surfaces and a family of strake thickness distributions were selected for the computational design study. The following equation describes the family of camber surfaces:

$$\bar{Y} = -\frac{\bar{X}_{\mathrm{LE}}}{\Theta_R}\left[1-\left(1-\frac{\bar{X}\Theta_R}{\bar{X}_{\mathrm{LE}}}\right)^{1/2}\right] \tag{1}$$

This is the equation for a family of circular arcs in a given spanwise plane (see Fig. 1) for the local $\bar{X}, \bar{Y}$ system. The origin of the $\bar{X}, \bar{Y}$ system is tied to the intersection of the strake with the forebody and therefore varies down the length of the body. The parameter $\bar{X}_{\mathrm{LE}}$ is the known location of the leading edge of the strake for each cross section (spanwise plane). The tip camber angle Θ_R, expressed in radians, is a user-specified variable that fixes the camber surface for analysis.

The following equation defines a thickness distribution that completes the construction of the surface of the strake:

$$\left(\frac{\bar{X}}{a}\right)^{2+\epsilon} + \left(\frac{\bar{Y}}{b}\right)^{2} = 1 \tag{2}$$

This is a modified elliptic equation where a is the local semimajor axis defined as the distance from the origin of the local $\bar{X}, \bar{Y}$ system to the $\bar{X}_{\mathrm{LE}}$ of each cross section. Similarly, b is the semiminor axis. The exponent ϵ is a user-specified variable that fixes the thickness distribution for analysis. This thickness distribution is then added vertically to the camber line to define the upper surface of the strake and subtracted vertically from the camberline to define the lower surface of the strake. Therefore, for each analysis of forebody-strake geometry, a value of Θ_R and ϵ is selected to complete the geometry specification. The resulting full-potential calculations are examined at several cross sections to determine if the attached-flow pressure distribution is achieved.

A typical result from the analysis study is shown in Fig. 1 for Mach 1.80 and $\alpha = 4$ deg. A cross section at 65% of the body length is examined for two different camberlines: $\Theta_R = 20$ and 40 deg for $\epsilon = -1.80$. The computed surface-pressure results are from the NCOREL full-potential code on a 57 × 57 grid. The computed surface pressures for these two cases illustrate an undesirable leading-edge suction spike for the $\Theta_R = 20$-deg case and a desirable pressure distribution for the $\Theta_R = 40$-deg case.

Computed results for two different thickness distributions at a cross section location 87% of body length are compared in Fig. 2. Values of $\epsilon = -1.00$ and -1.80, $\Theta_R = 40$ deg for Mach 1.80 and $\alpha = 4$ deg are shown. Both pressure distributions have basically the same characteristics and reflect the absence of large surface-pressure gradients near the tip. The $\epsilon = -1.80$ strake has a lower drag because of decreased volume. This strake would be expected to allow the flow to separate more easily as α is increased because of its smaller leading-edge radii.

The parametric evaluation of strake camber and thickness resulted in a design that was chosen for experimental validation. Values of $\Theta_R = 40$ deg and $\epsilon = -1.80$ were selected for all cross sections to define the strake. The particular thickness distributions represented by $\epsilon = -1.80$ were chosen because the research plan included an experimental investigation of the high α flowfield. Under high α conditions, a well-defined

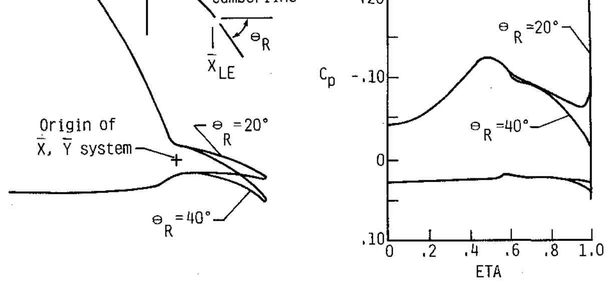

Fig. 1 Typical comparison of computed effect of variation in strake tip camber angle; $M = 1.80$, $\alpha = 4$ deg, $x/\ell = 0.65$, and $\epsilon = -1.80$.

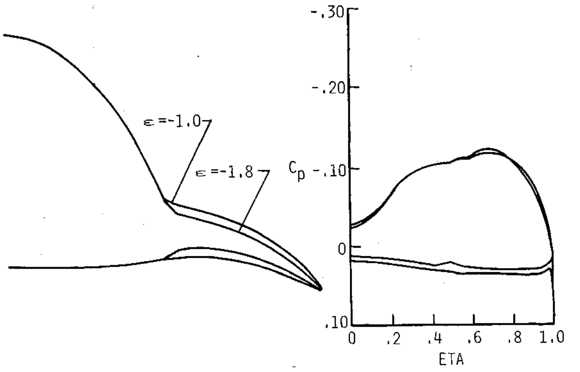

Fig. 2 Typical comparison of computed effect of variation in strake thickness envelope; $M = 1.80$, $\alpha = 4$ deg, $x/\ell = 0.87$, and $\Theta_R = 40$ deg.

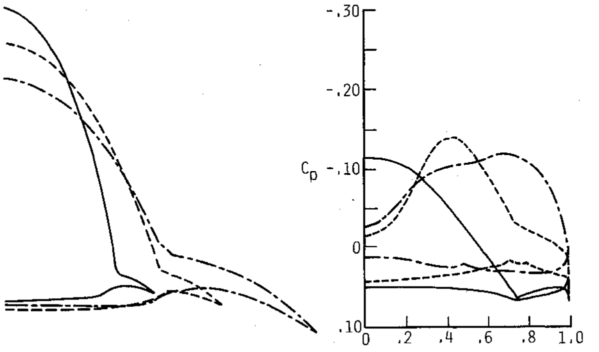

Fig. 3 Spanwise geometry definition and computed surface pressures for $M = 1.80$; $\alpha = 4$ deg; $x/\ell = 0.43$, 0.65, and 0.87, $\Theta_R = 40$ deg, and $\epsilon = -1.80$.

strake vortex was desired for study. Three cross sections from this geometry at forebody stations 43, 65, and 87% of body length are shown in Fig. 3 along with the calculated full-potential results. The strake does not produce lift initially, as evidenced by the nearly equal pressure on the upper and lower surfaces, but provides a significant lift force as the strake becomes larger. These three forebody stations were used as evaluation stations throughout the design study.

Experimental Verification Study

The transformation from a numerical model suitable for computational analysis to a physical model suitable for testing is a time-consuming task. Once the final forebody-strake design was established, a high-density numerical model was defined for wind-tunnel model design. Examination of the high-density numerical model indicated a wavy surface definition and an irregular intersection of the strake and forebody. Resolving these deficiencies in the surface definition required several man months. Also, the minimum leading-edge radius for an aluminum model is 0.0035 in. The leading-edge radius of the strake was increased on approximately the aft 50% of the strake to meet this requirement.

The forebody-cambered strake model was tested in the NASA Langley Unitary Plan Wind Tunnel[8] for Mach numbers of 1.60, 1.80, and 2.00 for a Reynolds number of 2×10^6/ft. The angle-of-attack range was from about 0 to 14 deg for a sideslip angle of 0 deg. Strips of transition-producing sand grit were placed 1.2 in. behind the nose of the model and 0.4 in. aft of the leading-edge of the strake to insure fully turbulent boundary-layer flow over most of the model surface. Surface-pressure data were obtained at three spanwise planes 43, 65, and 87% of body length or 15.0, 22.5, and 30.0 in. aft of the nose on a 34.5-in.-long model. Surface-pressure data were also obtained on the upper and lower centerlines. Force and moment data were obtained simultaneously with the pressure data. The force and moment data were corrected for sting bending caused by model loads and for tunnel flow angularity; the static pressure on the model base was adjusted to freestream conditions. Oil-flow and vapor-screen data were obtained subsequently. A photograph of the final forebody-cambered strake wind-tunnel model mounted in the NASA Langley Unitary Tunnel is presented in Fig. 4. The camera housing for obtaining vapor-screen photographs can be seen on the right side of the figure.

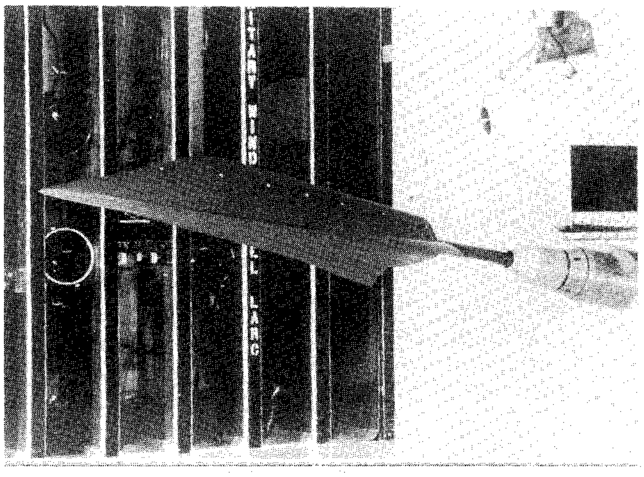

Fig. 4 Photograph of forebody-cambered strake model installed in NASA Langley Unitary Plan Wind Tunnel.

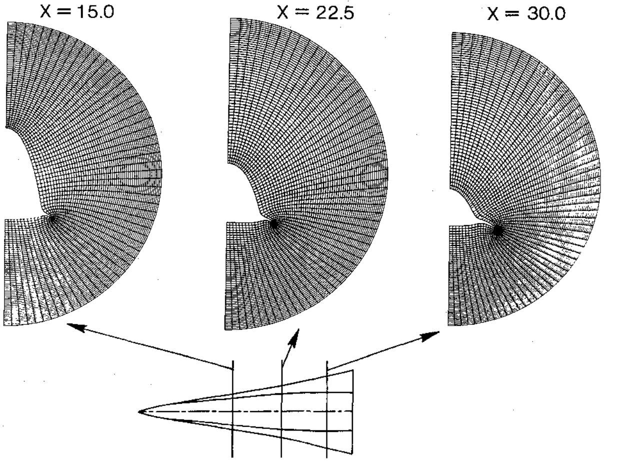

Fig. 5 Computation grid from NCOREL full-potential code; forebody-strake grids 57 × 57.

The design procedure is verified based on the following: 1) a comparison of the experimentally obtained surface-pressure data with the NCOREL calculations, and 2) an inspection of the low α oil-flow and vapor-screen flow-visualization data, which qualitatively shows the basic flow patterns. The NCOREL calculations were made on a 57×57 grid for 1-in. step sizes on a 34.5-in.-long model. The numerical model corresponded to the wind-tunnel model definition. Figure 5 presents the forebody-strake grids in the crossflow plane at the three data stations where the NCOREL calculations are compared with the experimental surface-pressure data.

The geometry of both the original design study model and the actual experimental test article for the three spanwise data stations are shown together in Figs. 6–8, respectively, to emphasize the changes that occurred in the wind-tunnel model design process. Also shown in these three figures are the surface-pressure distributions from the experiment and the NCOREL predictions for both the experimental wind-tunnel model and the design study model at three different α. Because of tunnel flow angularity, the design α of 4 deg was not achieved; therefore, the data shown are for $\alpha = 3.29$, 5.21, and 7.26 deg.

The data shown in Fig. 6 are for the forebody station 15 in. aft of the nose, or 43% of body length. The agreement between the experimental surface-pressure data and the NCOREL calculations for the experimental geometry is good except for the upper surface of the strake at $\alpha = 7.26$ deg. The vapor-screen photograph for this station and condition did not indicate flow separation, therefore, the attached-flow assumption of full-potential theory should be valid. The reason for the error is that the full-potential prediction is unknown. Note also that the NCOREL estimates for the design study and experimental geometries are in close agreement except for the strake upper surface.

The second data station is 22.5 in. aft of the nose, or 65% of body length, and is shown in Fig. 7. The agreement between the experimental surface pressures and the NCOREL calculations for that station is also good. The NCOREL calculations on the upper surface of the strake generally underpredict the expansion levels with a somewhat larger error at $\alpha = 7.26$ deg. NCOREL correctly computed the shock on the upper surface of the forebody at $\eta \approx 0.4$, but the computed position is somewhat inboard of the actual location. At $\alpha = 7.26$ deg, NCOREL overestimates the strength of this shock. The NCOREL computations were repeated on a 0.5-in. step size for the same crossflow grid density. A small improvement in the location of the forebody upper surface shock was found, but otherwise the computed results were generally unchanged. Notice that the changes in the design study and experimental geometries are reflected in the NCOREL-predicted surface pressures. The relatively small change in the forebody geometry significantly influenced the predicted strength of the forebody shock.

The final spanwise data station, shown in Fig. 8, is 30 in. aft of the nose, or 87% of body length. The overall quality of the NCOREL pressure estimates is similar to that shown previously. In particular, the NCOREL calculations for the strake upper surface are in very good agreement with experimental data except for the local region where the strake and forebody intersect near $\eta = 0.5$. A comparison of the two geometries shows that changes caused by the wind-tunnel model design process were fairly significant at this station.

A plot of the centerline geometry of the forebodies from the design study and the experimental model is shown in Fig. 9 along with the corresponding pressure data. Waviness on the upper surface centerline aft of the canopy is apparent. The effect of this waviness can be seen in the calculated centerline pressures at all α. The small changes to the geometry on the nose and canopy regions have a surprisingly large effect on the pressure calculations.

Comparing the NCOREL pressure estimates for the experimental geometry and the experimentally obtained pressure data shows good agreement, except for the upper surface centerline aft of 60% of body length. For all three α, the computed centerline pressures in this region are more positive than the experimental pressures. The difference between computed and experimental pressures in that region increases with increasing α. This error in the full-potential calculation on the top centerline aft of the canopy was also shown in a figure presented in Ref. 9 for a similar geometry and computational method. No explanation for the difference was offered in that publication.

A photograph of the experimentally determined upper surface streamlines as indicated by the oil-flow technique is shown in Fig. 10. The angle of attack is roughly 4 deg. The flow pattern is basically smooth without any indication of upper surface flow separation except for the centerline region aft of the canopy. In this region, the classic herringbone pattern that occurs under a vortex is noted on either side of the centerline. The pair of symmetric vortices on either side of the centerline and aft of the canopy is the likely source of the discrepancy between full-potential and experimental pressures. It is believed the upper surface shock noted at $x = 22.5$ in. causes these vortices.

A vapor-screen photograph of the upper surface flowfield near the trailing edge at $\alpha \approx 7$ deg is shown in Fig. 11. The

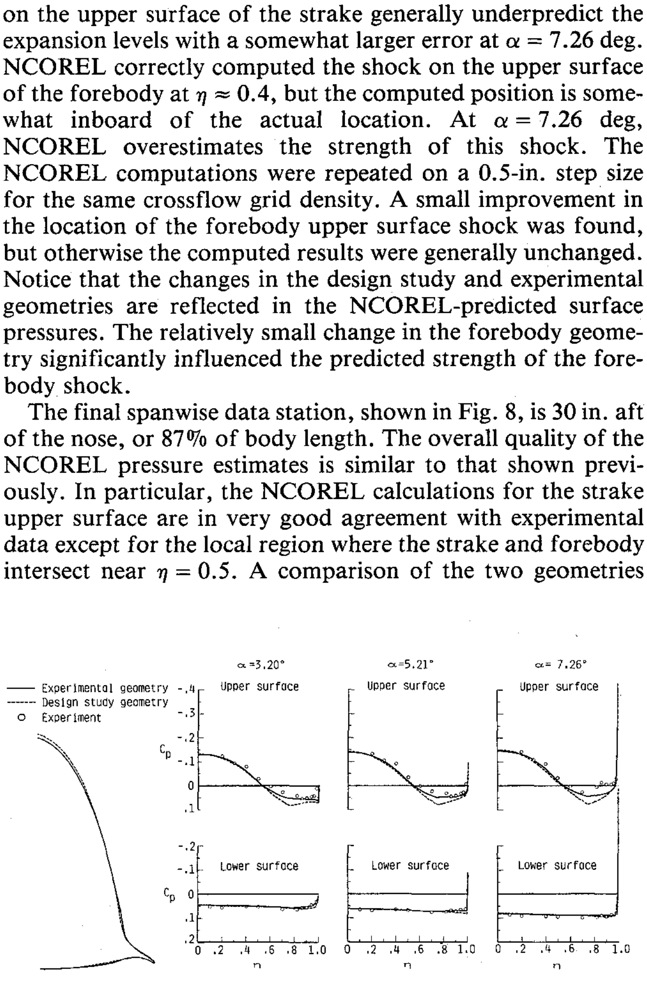

Fig. 6 Comparison of design study with actual wind-tunnel geometries, NCOREL-computed pressure distributions, and experimental data at $x = 15$ in. and $M = 1.80$.

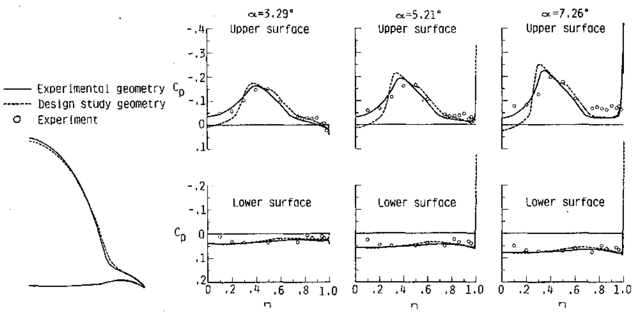

Fig. 7 Comparison of design study with actual wind-tunnel geometries, NCOREL-computed pressure distributions, and experimental data at $x = 22.5$ in. and $M = 1.80$.

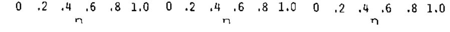

Fig. 8 Comparison of design study with actual wind-tunnel geometries, NCOREL-computed pressure distributions, and experimental data at $x = 30$ in. and $M = 1.80$.

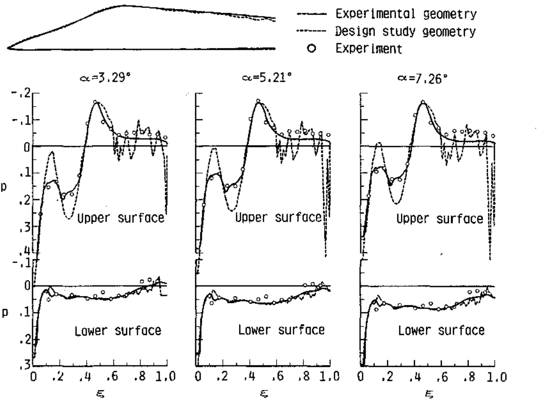

Fig. 9 Comparison of design study with actual wind-tunnel geometries, NCOREL-computed pressure distributions, and experimental data at $Y = 0.0$ in. and $M = 1.80$.

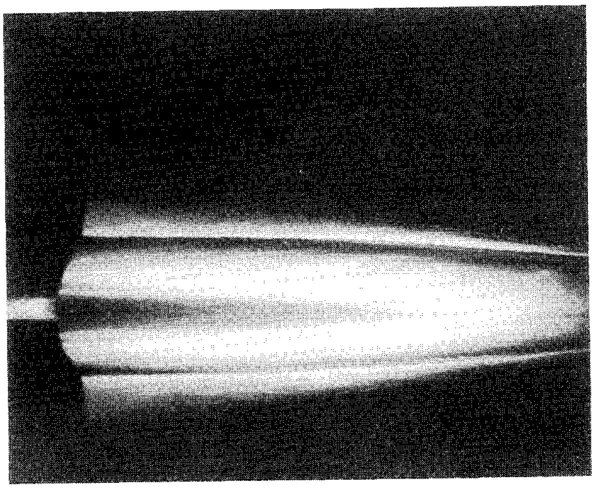

AFT SECTION

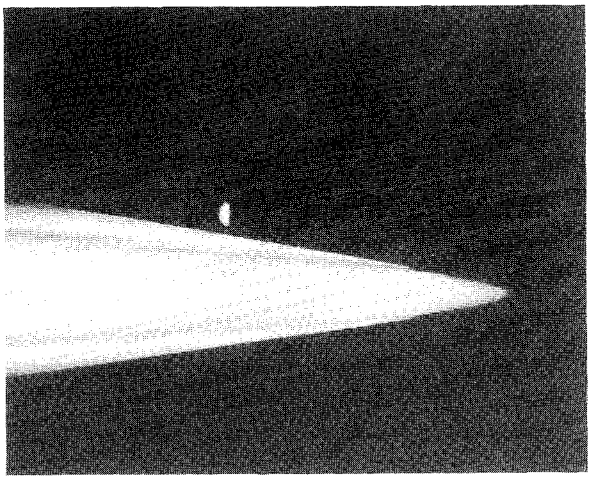

FORE SECTION

Fig. 10 Oil flow on the upper surface; $M = 1.80$, $\alpha \approx 4$ deg.

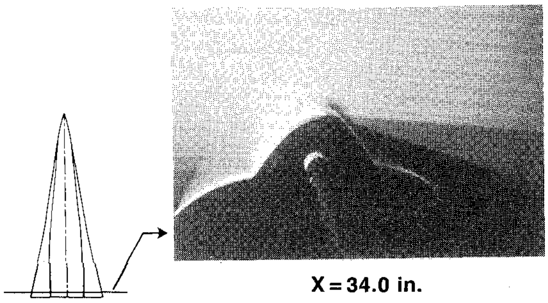

Fig. 11 Vapor screen for $M = 1.80$, $\alpha \approx 7$ deg, $x = 34$ in.

observer is behind the model looking forward. The light source is on the left side of the model. According to the vapor-screen technique, the flow over the strake upper surface is attached, i.e., a leading-edge vortex does not form. However, a pair of vortices on the forebody upper surface centerline can be seen. The forebody vortices are indicated by the herringbone pattern of the oil-flow presented in Fig. 10. These vortices could be identified for α as low as 2 deg.

High Alpha Flowfield

The computational study focused on low α where the flowfield is expected to remain attached over the geometry. However, during the experimental verification study, the high α flowfield was also investigated. In the preceding section, it was noted that an attached flowfield on the upper surface of the

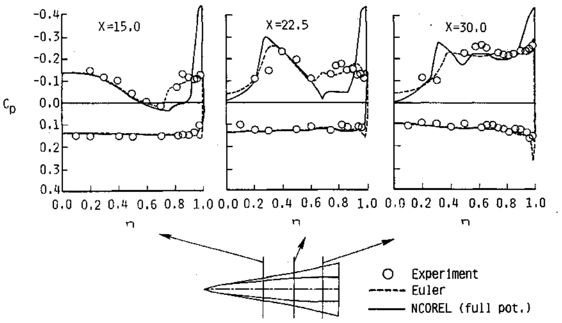

Fig. 12 Comparison of full-potential and Euler results with experimental pressure data at $M = 1.80$ and $\alpha = 11.29$ deg.

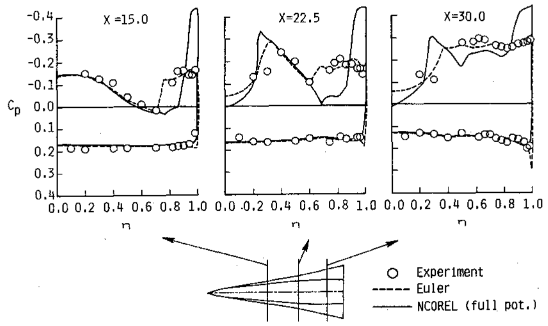

Fig. 13 Comparison of full-potential and Euler results with experimental pressure data at $M = 1.80$ and $\alpha = 13.27$ deg.

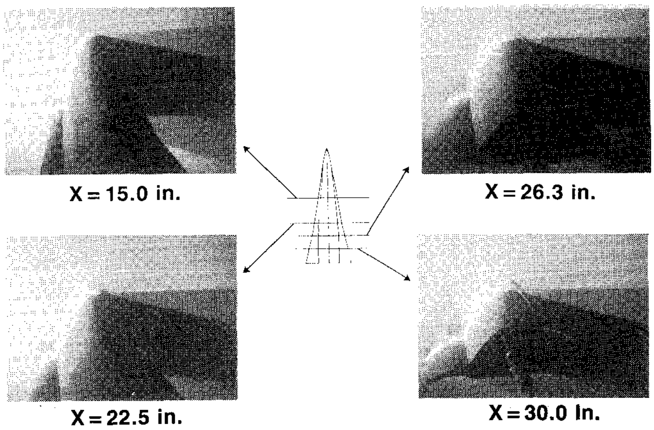

Fig. 14 Vapor screens for $M = 1.80$, $\alpha \approx 13$ deg, $\beta = 0$ deg.

strake was found for an α as high as roughly 7 deg. However, for an additional α of approximately 2 deg, a leading-edge vortex was observed in the vapor screens.

The full-potential equation cannot model the separated regions of the flowfield. An Euler solver can model rotationality in inviscid flow but cannot model the separation mechanism that is a viscous effect. However, for a sharp leading-edge lifting surface, an Euler solver can model the primary leading-edge vortex.[4,5] A recently developed Euler solver[10] was used to calculate the flow on the forebody-cambered strake geometry. The results shown in Figs. 12 and 13 compare the experimental pressure data for three spanwise locations with full-potential and Euler calculations at $M = 1.80$ and $\alpha = 11.29$ and 13.27 deg, respectively.

The results given for both methods are for a 1-in. marching step size and a 57 × 57 grid for the full-potential method and a 68 × 57 grid for the Euler method. Both methods correctly compute the pressure distribution on the lower body and strake surfaces, and, in fact, the full-potential and Euler results are virtually identical in this region. This is direct evidence that the losses in stagnation pressure through the bow shock are small for this Mach number α combination.

However, the computed results on the upper surface of the strake are significantly different. The full-potential method predicts a leading-edge overexpansion to the vacuum limit, which recompresses sharply through a crossflow shock just inboard of the leading edge. Experimental evidence does not support this flowfield structure. On the other hand, the Euler results agree very well with the experimental pressures on the upper surface of the strake. Examining the Euler-predicted velocity vectors clearly showed a leading-edge vortex flow on the leeside of the strake. Two entirely different predicted flowfields on the strake upper surface, i.e., an attached flow field with strong crossflow shock from the full-potential method and a leading-edge vortex flow from the Euler method, do not seem to significantly affect the computed pressures on the upper surface of the forebody as indicated by the agreement between the full-potential and Euler results in this region. At $x = 22.5$ and 30 in., both methods predict an embedded flowfield shock that is also indicated in the experimental surface pressures at $\eta \approx 0.2$. This embedded shock is stronger in the full-potential calculations than in the Euler results.

An additional comparison of full-potential and Euler calculations with experimental surface-pressure data for the three spanwise data stations at $M = 1.80$ and $\alpha = 13.27$ deg is shown in Fig. 13. The statements made in the preceding paragraph for the $\alpha = 11.29$ deg case also apply to the results at this α, as expected. The trends of the comparisons between the full-potential and Euler methods with the experimental data are unchanged. The pressure drop across the two embedded shocks predicted by full-potential theory is slightly larger at this higher α, but the expansion pressure at the leading edge is unchanged since the pressure plateau increased at $\alpha = 13.27$ deg. The Euler method predicts a slightly stronger leading-edge vortex as evidenced by the more negative pressure coefficients. The embedded flowfield shock is also stronger at the higher α.

The complex nature of the high α flowfield can be seen from the vapor-screen photographs presented in Fig. 14. Four photographs are presented at $x = 15$, 22.5, 26.3, and 30 in. for $\alpha \approx 13.1$ deg, $\beta = 0$ deg. In each of the four photographs, the large vortex on the upper surface of the strake can be clearly seen. The vortex core is well defined as is the feeding sheet that originates from the leading edge. The pair of symmetric vortices previously noted in Fig. 11 on the upper surface of the forebody at $\alpha \approx 7$ deg are, of course, still present. An embedded flowfield shock is visible on the upper surface of the forebody for three of the stations. The most forward station, $x = 15$ in., is near the maximum height of the canopy. An embedded shock is not apparent at this station. The next photograph is $x = 22.5$ in., just aft of the canopy, where an embedded shock is faintly visible well up on the body side. The separated region has formed on either side of the centerline as evidenced by the two dark regions. At station $x = 26.3$ in., the photograph again indicates the strake vortex, the pair of centerline vortices, and now a more clearly defined embedded shock. Note that the position of the shock has moved about halfway down the side of the body. The final vapor-screen photograph at $x = 30$ in. shows that the embedded shock continues to move outboard and now interacts with the strake vortex.

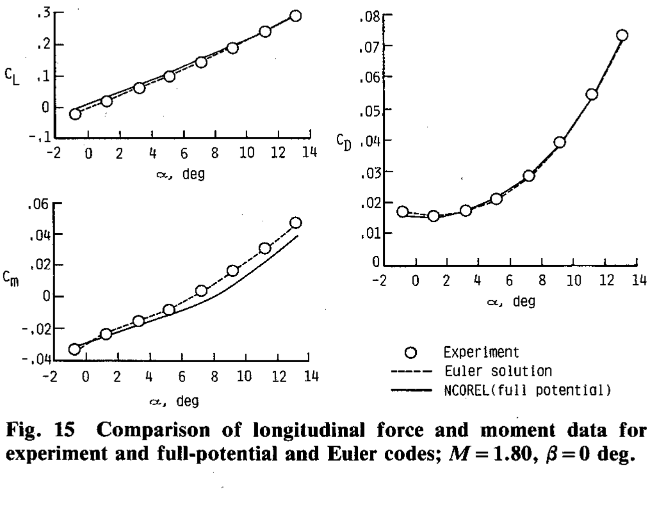

Fig. 15 Comparison of longitudinal force and moment data for experiment and full-potential and Euler codes; $M = 1.80$, $\beta = 0$ deg.

Longitudinal Force and Moment Comparison

A comparison of lift, drag, and pitching-moment coefficients from the full-potential and Euler codes with the experimental data is shown in Fig. 15. The drag comparison includes a constant skin friction drag coefficient of 0.0071 from the method used in Ref. 11, which is added to the full-potential and Euler inviscid drag coefficients. These coefficients are well computed by both methods, however, the Euler results are clearly superior. The Euler results showed that, for this particular geometry with a highly cambered strake, a region of leading-edge vorticity developed on the lower surface of the strake at low α. This is the primary difference between the full-potential and Euler results at low α.

At high α conditions, the lift and drag estimates are virtually identical and agree well with the experimental data. However, the pitching moment prediction from the Euler solver is significantly improved over the full-potential results and is in excellent agreement with the experiment. Based on the comparisons of surface-pressure data, the close agreement between full potential and Euler lift and drag is somewhat surprising.

Conclusions

A procedure for the design of strake camber and thickness in supersonic flow at low lift mounted on a large forebody has been developed and verified through an experimental test program. The goal of the design effort was to maintain an attached flowfield on the upper surface of the strake at the low α conditions typical of cruise. The design procedure used a full-potential supersonic marching code, which accurately computed the flowfield on a complex forebody-strake geometry. An empirical guideline coupled with the accurate surface-pressure calculation from the NCOREL full-potential code was used to determine the strake surface contours that yielded attached flow at the design point.

Typical results of the computational design study were presented to describe the details of the geometry development. As a result of this study, a cambered strake-forebody design was selected for model fabrication. The experimental test program, which consisted of force and moment, surface-pressure, and flow-visualization data, confirmed that the design criterion of attached flow on the strake was met for the design conditions of Mach 1.80 and $\alpha \approx 4$ deg.

The high α flowfield was also investigated both experimentally and computationally. Vapor-screen data indicated the presence of a large, well-defined strake vortex that filled the strake-forebody intersection region for α approximately ≥ 9 deg. Additionally, an embedded shock, which was indicated in the surface-pressure data and visible in the vapor-screen data, formed on the upper surface of the forebody aft of the canopy for α approximately >2 deg. This shock apparently caused flow separation that evolved into a pair of symmetric vortices) also clearly evident in the vapor-screen and oil-flow data).

Surface-pressure data were compared to full-potential and Euler code results to assess the validity of each method for high α conditions. The full-potential equation does not model the physics of a separated flowfield and, therefore, good agreement is not expected in separated regions. However, the full-potential method predicted the surface pressures well in the attached flowfield at high α.

Overall agreement between experimental surface-pressure data and Euler predictions was excellent. The Euler method correctly predicted the occurrence of a strake vortex at $\alpha = 11.29$ and 13.27 deg. It is believed that the numerical artificial viscosity in the Euler method and the sharp leading edge of the strake cause a leading-edge vortex to form in the inviscid computation. The only significant error in the Euler surface-pressure predictions was in the region of the forebody upper surface aft of the canopy. The Euler method computed the embedded shock but not the vortices that formed aft of the embedded shock.

Experimental lift, drag, and pitching-moment data were compared with both the full-potential and Euler predictions across the α range. Both methods accurately predicted the experimental lift and drag data but the Euler calculations are superior. The Euler preditions of pitching moment were clearly superior to those of the full-potential method.

References

[1]Lamar, J. E., "Nonlinear Lift Control at High Speed and High Angle of Attack Using Vortex Flow Technology," AGARD Rept. No. 740, Oct. 1987, pp. 4-1-4-23.

[2]Meyer, R. C., and Fields, W.D., "Configuration Development of a Supersonic Cruise Strike-Fighter," AIAA Paper 78-148, Jan. 1978.

[3]Siclari, M. J., "An Improved Version of NCOREL. A Computer Program for 3-D Nonlinear Supersonic Potential Flow Calculations," NASA CR-4165, July 1988.

[4]Newsome, R. W., and Kandil, O. A., "Vortical Flow Aerodynamics—Physical Aspects and Numerical Simulation," AIAA Paper 87-0205, Jan. 1987.

[5]McMillin, S. N., Thomas, J. L., and Murman, E. M., "Euler and Navier-Stokes Solutions for the Leeside Flow Over Delta Wings at Supersonic Speeds," AIAA Paper 87-2270, Aug. 1987

[6]Miller, D. S., Landrum, E. J., Townsend, J. C., and Mason, W. H., "Pressure and Force Data for a Flat Wing and a Warped Conical Wing Having a Shockless Recompression at Mach 1.62," NASA TP-1759, 1981.

[7]Pittman, J. L., Miller, D. S., and Mason, W. H., "Supersonic, Nonlinear Attached Flow Wing Design for High Lift with Experimental Validation," NASA TP-2336, 1984.

[8]Jackson, C. M., Jr., Corlett, W. A., and Monta, W. J., "Description and Calibration of the Langley Unitary Plan Wind Tunnel," NASA TP-1905, 1981.

[9]Walkley, K. B., and Smith, G. E., "Application of a Full Potential Method to Practical Problems in Supersonic Aircraft Design and Analysis," *Proceedings of 15th Congress of the International Council of the Aeronautical Sciences*, Vol. 1, edited by P. Santini and R. Staufenbiel, AIAA, New York, 1986, pp. 491-501.

[10]Siclari, M. J., and Del Guidice, P., "A Hybrid Finite Volume Approach to Euler Solutions for Supersonic Flows," AIAA Paper 87-1463, 1987.

[11]Sommer, S. C., and Short, B. J., "Free-Flight Measurements of Turbulent-Boundary-Layer Skin Friction in the Presence of Severe Aerodynamic Heating at Mach Numbers from 2.8 to 7.0," NACA TN-3391, March 1955.